Soft Matter

PAPER

View Article Online
View Journal | View Issue

Cite this: *Soft Matter*, 2025, **21**, 982

Influence of the neck length of urease-powered flask-like colloidal motors on their kinematic behavior†

Chang Zhou,[ab] Yingjie Wu,[*a] Tieyan Si,[a] Kangning Zhu,[b] Mingcheng Yang[*cde] and Qiang He[*a]

Received 4th November 2024,
Accepted 30th December 2024

DOI: 10.1039/d4sm01294a

rsc.li/soft-matter-journal

Enzyme-powered synthetic colloidal motors hold promising potential for *in vivo* medical applications because of their unique features such as self-propulsion, sub-micrometer size, fuel bioavailability, and structural and functional versatility. However, the key parameters influencing the propulsion efficiency of enzyme-powered colloidal motors still remain unclear. Here, we report the effect of the neck length of urease-powered pentosan flask-like colloidal motors on their kinematic behavior resembling the role of bacterial flagella. The sub-micrometer-sized and streamlined pentosan flask-like colloidal motors with variable neck lengths are synthesized through a facile interfacial dynamic assembly and polymerization strategy. The urease molecules are loaded through vacuum infusion technology and thus the urease-triggered catalytic reaction can propel the pentosan flask-like colloidal motors to move autonomously in the urea solution. The self-propelled speed of these pentosan flask-like colloidal motors significantly increases with the elongating neck lengths. The mechanism of the relationship between the neck length and self-propelled motion is that a longer neck can provide a larger self-propelled force due to the larger force area and stabilize the rotation because of the increased rotational friction. This research can provide guidance for the design of biomedical colloidal motors.

1. Introduction

Living microorganisms such as bacteria autonomously move in the complex environment at an exceedingly low Reynolds number; thus, their motion is independent on inertia. For instance, motile bacteria rotate their flagella filaments to break symmetry and obtain kinetic energy to swim. In this context, many factors which can affect the self-propelled motion have been studied such as flagella's length. It is found that the bacteria with short flagella have larger rotational diffusion, which can reorient them fast to find the direction of nutrition gradients; however, the strong rotation would reduce the bacteria's ability to follow a gradient efficiently. By comparison, those bacteria with longer flagella can increase drag to better stabilize the direction of motion so that the bacteria can reduce the dissipation of energy for their chemotaxis, adapting the complex environments to survive.[1,2] Inspired by motile bacteria, researchers have established various colloidal motors that can convert chemical fuels[3–8] or external energy (*e.g.*, ultrasonic,[9,10] optical[4,11] and magnetic[12,13] fields) into mechanical work. These synthetic colloidal motors with self-propulsion can pass through various biological barriers such as the mucus barrier[14] or the tumor interstitial pressure[15,16] to reach the deep region of the lesion site, exhibiting the potential in the field of precision medicine.[17–25] To this end, they should at least possess specific features including sub-micrometer sizes, biocompatibility and biodegradability of fabrication materials and fuels, high drug loading volume, higher energy conversion, and controllable motion in biological media.[26–33] Recently, enzyme-powered flask-like colloidal motors capable of meeting the above-mentioned requirements have attracted much attention for practical biomedical applications.[34,35] However, the exact role of their flask-like architecture in the conversion of chemical to mechanical energy and the precise control of motion is still unclear.

Herein, we prepared sub-micrometer-sized, streamlined and urease-powered pentosan flask-like colloidal motors with

[a] *School of Medicine and Health, Harbin Institute of Technology, XiDaZhi Street 92, Harbin, 150001, China. E-mail: qianghe@hit.edu.cn, wuyingjie@hit.edu.cn*
[b] *Wenzhou Institute, University of Chinese Academy of Sciences, Jinlian Street, Wenzhou, 325000, China*
[c] *Beijing National Laboratory for Condensed Matter Physics and Laboratory of Soft Matter Physics, Institute of Physics, Chinese Academy of Sciences, Beijing, 100190, China. E-mail: mcyang@iphy.ac.cn*
[d] *School of Physical Sciences, University of Chinese Academy of Sciences, Beijing, 100049, China*
[e] *Songshan Lake Materials Laboratory, Dongguan, Guangdong 523808, China*

† Electronic supplementary information (ESI) available. See DOI: https://doi.org/10.1039/d4sm01294a

different neck lengths and the same hollow round bottom to investigate the effect of flask-like architecture on their kinematic behavior. These pentosan flask-like colloidal motors powered by the hydrolysis of urea catalyzed by urease in the hollow cavity can move autonomously. It is found that at identical reaction rates, the self-propelled velocity increases with the lengthening neck because of the increased self-propelled force. Meanwhile, the stochastic rotation of the pentosan flask-like colloidal motors with a longer neck length is suppressed because of the increased rotational friction. The faster and straighter movement of the longer-necked pentosan flask-like colloidal motors is owing to the increasing translational energy efficiency. The numerical simulation of the self-propelled force and velocity as well as fluid flow field analysis around three kinds of pentosan flask-like colloidal motors reveals that the longer neck length can increase the self-propelled force along the moving direction due to the increased force area, whereas the translational drag slightly changes, which increases the self-propelled velocity and the straightness of the self-propelled motion.

2. Experimental

2.1. Materials

Sodium oleate (SO), poly(ethylene glycol)-*block*-poly(propylene glycol)-*block*-poly-(ethylene glycol) (EO_{20}–PO_{70}–EO_{20}, P123), D-ribose, urease, phosphate buffer saline (PBS), uranyl acetate, *P*-nitrophenol and urea were purchased from Sigma-Aldrich. All chemicals were used without further purification. Ultrapure water (Millipore) of 18.2 MΩ cm was used for all experiments.

2.2. Preparation of the pentosan flask-like colloidal motors with different neck lengths

Pentosan flask-like colloidal motors were synthesized according to a previous method.[31] Briefly, 0.0365 g of SO and 0.0435 g of P123 were added into 20 mL of deionized water and stirred slowly to form a clear solution. Then, 40 mL of solution containing 3 g of D-ribose was added into the above solution. After stirring for 30 min, the solution was transferred to a 100 mL autoclave and then the autoclave was placed in an oven at 160 °C. After 9 h, short-necked N100nm pentosan flask-like colloidal particles were collected and washed by centrifugation. After this, the short-necked N100nm pentosan flask-like colloidal particles were dried and stored. Then, 0.5 mg of the short-necked N100nm pentosan flask-like colloidal particles were added into 1 mL of solution containing 10 mg of urease. The above solution was then placed in a vacuum chamber at a pressure of −1 × 105 Pa. Then, the dispersion was ultrasonically dispersed for 1 h. The short-necked N100nm pentosan flask-like colloidal motors were washed by centrifugation using PBS solution (pH = 7.2). Finally, the short-necked N100nm pentosan flask-like colloidal motors were collected and stored at 4 °C. The medium N300nm and long-necked N600nm pentosan flask-like colloidal motors were obtained using the same method except that the time of the hydrothermal process was changed to 10 and 11 h, respectively.

2.3. Optical video recording

The self-propelled motion of the pentosan flask-like colloidal motors was observed using an Olympus IX71 inverted microscope with a CCD camera. The pentosan flask-like colloidal motors were added into the urea solution first and the dispersion was added on a clear glass. The glass was sealed by cover glass to minimize the flow effect. The thickness of the solution between the slide and the coverslip was about 10 μm. As the flask-like colloidal motors were about 500 nm, there was enough volume for the observation of the flask-like colloidal motors. On the other hand, it is ensured that the amount of the flask-like colloidal motors is 5–10 in an area of 200 μm × 400 μm.

3. Results and discussion

3.1. Fabrication and characterization

Urease-powered pentosan flask-like colloidal motors with variable neck lengths were prepared according to a previously reported method[36] with some modifications as schematically illustrated in Fig. 1a. Briefly, two surfactants, poly(ethylene glycol)-*block*-poly(propylene glycol)-*block*-poly-(ethylene glycol) ($EO_{20}PO_{70}EO_{20}$, P123) and sodium oleate, were dissolved in deionized water to prepare the mixed micelles as the soft templates. After D-ribose was added, the mixture was transferred to an autoclave and hydrothermally treated at 160 °C. With the

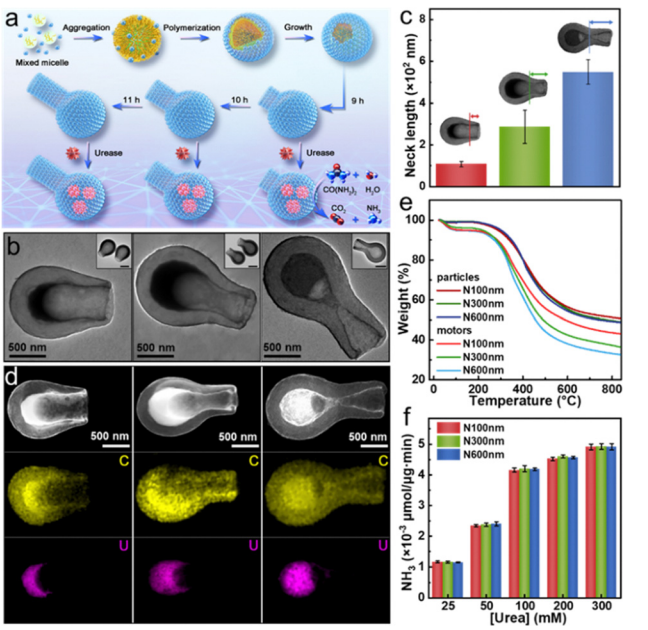

Fig. 1 Characterization of urease powered pentosan flask-like colloidal motors. (a) Scheme of the preparation of pentosan flask-like colloidal motors. (b) TEM images of the flask-like colloidal motors with different neck lengths. The insets in (b) are the TEM images of the corresponding pentosan flask-like colloidal particles. (c) The measurement of the neck length of different pentosan flask-like colloidal particles. (d) STEM images and corresponding EDX images for element analysis of the pentosan flask-like colloidal motors. (e) TGA plots of the pentosan flask-like colloidal motors and particles with different neck lengths. (f) The reaction rate of the pentosan flask-like colloidal motors in different urea concentrations.

polymerization of D-ribose monomers at the interface, these micelle templates started to swell, which accompanied the polysaccharide polymer pentosan shell cracking. Meanwhile, the micelle templates spilled from the cracked region and thus the polymerization occurred at the new interface to form the neck of the pentosan flask-like colloidal particles. Finally, the different neck lengths could be prepared by controlling the hydrothermal times for 9, 10, and 11 h, respectively. The transmission electron microscopy (TEM) images in Fig. 1b illustrate that the three kinds of as-synthesized colloidal motors with hydrothermal synthesis times of 9 h, 10 h, and 11 h possess uniform round-bottom flask morphology with a streamlined spherical bottom and bottleneck. The outer diameters of the streamlined bottom and the neck opening are 700 ± 50 nm and 350 ± 33 nm. A hollow cavity can be clearly observed in these pentosan flask-like colloidal motors, in which the inner diameter on the hollow cavities of these motors is 550 ± 80 nm. By comparison, the inner diameter of their neck openings gradually reduces from 300 ± 43 nm to 120 ± 23 nm as the increasing neck lengths. Interestingly, the statistical analysis in Fig. 1c shows that the neck lengths of these pentosan flask-like colloidal motors are 107.6 ± 13.4 nm (denoted as N100nm), 286.2 ± 79.2 nm (denoted as N300nm), and 548.5 ± 57.3 nm (denoted as N600nm), which are corresponding to the hydrothermal synthesis times of 9 h, 10 h, and 11 h, respectively. This demonstrates that the neck length of these pentosan flask-like colloidal motors can be varied by tuning the hydrothermal polymerization time.

To better indicate the existence of enzymes using TEM, the urease was positively stained by uranyl acetate ($UO_2(CH_3COO)_2 \cdot 2H_2O$) to enhance its contrast.[37] In comparison to the inset in Fig. 1b, it can be found that dark regions appeared in the hollow cavities of the obtained pentosan flask-like colloidal motors. Furthermore, scanning transmission electron microscopy (STEM) equipped with energy-dispersive X-ray spectroscopy (EDX) in Fig. 1d displays the uranium (U: magenta) distribution, exactly overlapped with the dark regions of TEM images as shown in Fig. 1b, indicating the successful loading of urease inside the pentosan flask-like colloidal particles. Particularly, the TEM and STEM images along with corresponding EDX spectra demonstrate that the urease molecules mainly distribute in the hollow cavities and thus the urease-catalyzed reaction can be considered occurring inside the pentosan flask-like colloidal motors. Besides, the amount of the urease loaded inside the three kinds of pentosan flask-like colloidal motors is measured by thermogravimetric analysis (TGA) as shown in Fig. 1e. The TGA plots show the amount of the urease loaded inside the N100nm, N300nm and N600nm pentosan flask-like colloidal motors is about 7.57 wt%, 12.54 wt% and 16.12 wt%, respectively. More particularly, the enzymatic reaction rate of three kinds of pentosan flask-like colloidal motors is evaluated by using the titrimetric method.[38] The results in Fig. 1f illustrate the identical reaction rate of three kinds of pentosan flask-like colloidal motors in different urea concentrations, suggesting that the neck lengths have neglectable effect on the reaction rate at the same substrate concentrations. Hence, the only difference among three types of urease-powered pentosan flask-like colloidal motors lies in the variable neck lengths, which is crucial for researching the influence of colloidal motor's nanoarchitectures on their self-propulsion behavior.

3.2. Self-propelling motion analysis

The self-propelling motion of shorted-necked (N100nm), medium-necked (N300nm), and long-necked (N600nm) urease-powered pentosan flask-like colloidal motors was examined by employing optical microscopy in the 25 mM urea solution for 2 s. The time-lapse images show that three kinds of urease-powered pentosan flask-like colloidal motors autonomously move with opening forward (Fig. 2a, taken from Videos S1–S3, ESI†). Interestingly, the pentosan flask-like colloidal motors tend to move along a straight trajectory with increasing neck lengths, in which the N100nm, N300nm and N600nm pentosan flask-like colloidal motors show the tumbling, turning and ballistic motions, respectively. The longer motion of the pentosan flask-like colloidal

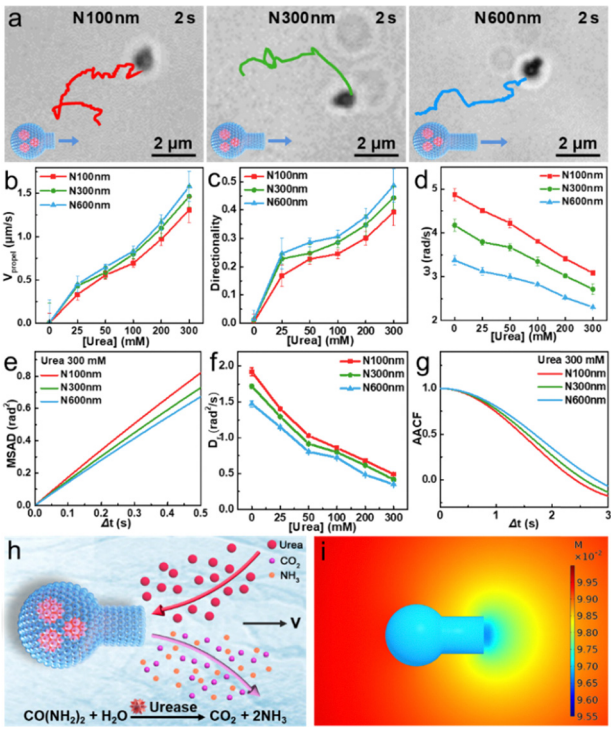

Fig. 2 Self-propelled motion of pentosan flask-like colloidal motors. (a) Time lapse images of the self-propelled motion of the pentosan flask-like colloidal motors with different neck lengths in the 25 mM urea solution for 2 s. (b) The self-propelled velocity of the pentosan flask-like colloidal motors with different neck lengths in different urea concentrations. (c) The directionality ($\cos\theta$) of the self-propelled motion of the pentosan flask-like colloidal motors in the solution with different urea concentrations. (d) The angular velocity of the pentosan flask-like colloidal motors with different neck lengths dependent on different urea concentrations. (e) MSAD curves of the pentosan flask-like colloidal motors with different neck lengths as a function of Δt in 300 mM urea solution. (f) Rotational diffusion coefficient of the pentosan flask-like colloidal motors with different neck lengths in different urea concentrations. (g) AACF of the pentosan flask-like colloidal motors with different neck lengths in 300 mM urea solution. (h) The scheme of the reaction occurring in the pentosan flask-like colloidal motor. (i) The simulation of the urea concentration distribution around the pentosan flask-like colloidal motor.

motors with different neck lengths shows that the N100nm pentosan flask-like colloidal motors will rotate quickly with the undirected motion, while the N300nm pentosan flask-like colloidal motors rotate slower and N600nm the slowest, which suggests that the pentosan flask-like colloidal motors can move with more directionality (Videos S4–S6, ESI†). Besides, the self-propelled motion of multiple pentosan flask-like colloidal motors shows that the pentosan flask-like colloidal motors with a specific neck length have similar motion behavior (Videos S7–S9, ESI†). To better understand the underlying mechanism, the self-propelling velocity was analyzed according to the schematic illustration in Fig. S1 (ESI†). The direction from the round bottom to the opening of the pentosan flask-like colloidal motors is set as the direction vector, and thus the self-propelling velocity is defined as the velocity projected in the direction vector. Also, there is a deviation angle θ between the apparent moving direction and the direction vector. In this case, the self-propelling velocity is calculated as follows:

$$v_{\text{propel}} = v_{\text{ACT}} \times \cos\theta \quad (1)$$

where v_{propel} is the self-propelling velocity of urease-powered pentosan flask-like colloidal motors, v_{ACT} is the apparent velocity which is calculated by the ratio of the total distance to the total time in one frame. Fig. 2b shows that the self-propelling velocity of three kinds of urease-powered pentosan flask-like colloidal motors in the absence of urea is equal to 0 μm s^{-1}. It is noted that here the self-propelling velocity excludes the contribution of the Brownian motion. Then, the self-propelling velocity of three kinds of pentosan flask-like colloidal motors went up with the increasing urea concentration. Interestingly, in the same urea concentration, the self-propelling velocity of the long-necked N600nm motor is approximately 11.12% faster than the medium-necked N300nm and 36% than the short-necked N100nm. In other words, the self-propelling forces positively correlate with the neck lengths of pentosan flask-like colloidal motors. Furthermore, $\cos\theta$ is defined as directionality to comparatively analyze the trajectories of pentosan flask-like colloidal motors.[39] It can be easily deduced that the pentosan flask-like colloidal motors moving along the axial direction can have a directionality of 1 (*i.e.* $\cos 0$) for the forward movement and -1 ($\cos\pi$) for the backward movement. If a pentosan flask-like colloidal motor moves along a straight path, $\cos\theta$ should be close to 1. Fig. 2c shows that the directionality of the long-necked N600nm motors is roughly 15% larger than the medium-necked N300nm and 65% than the short-necked N100nm in the same urea concentration. In contrast, the directionality of the Brownian motion in the absence of urea fuels is equal to 0. Besides, the effect of the neck lengths on the rotational motion of pentosan flask-like colloidal motors in different urea concentrations is also examined. Fig. 2d displays that the randomly rotational speed ω of three kinds of pentosan flask-like colloidal motors gradually declines with the increasing urea concentrations. In particular, the long-necked N600nm motors rotate about 19% slower than the medium-necked N300nm and 31% more than the short-necked N100nm at the same urea concentration. Further analysis of the mean square angular displacement (MSAD) as a function of time interval shows that the longer-necked pentosan flask-like colloidal motors have lower rotational diffusion ability (Fig. 2e). For instance, the short-necked N100nm motors have the largest value of MSAD at 300 mM urea solution. In addition, the rotational diffusion coefficient D_r in different urea concentrations is calculated as shown in Fig. 2f. It can be found that, for the Brownian motion, the D_r decreases from 1.92 $\pm$ 0.05 to 1.09 $\pm$ 0.15 $rad^2\ s^{-1}$ corresponding to the short-necked N100nm motors and the long-necked N600nm motors. It follows the Stokes–Einstein–Debye (SED) relationship, indicating that the larger particles have smaller rotational diffusion. The D_r of the self-propelled motion in the solution with different urea concentrations is inversely proportional to the neck lengths. The D_r of the short-necked N100nm decreases about 8.55% to the medium-necked N300nm and at most 20.94% to that of the long-necked N600nm. It can be explained as the larger particles have a larger friction coefficient, which can reduce the rotational ability under the same conditions. The influence of the neck length of pentosan flask-like colloidal motors on their reorientation was further analyzed using an angular autocorrelation function (AACF),[40]

$$\text{AACF} = \langle e_{v_t} \cdot e_{v_0} \rangle \quad (2)$$

where e_{v_t} and e_{v_0} are the unit vector of the self-propelling velocity at time t and 0. It can be easily derived that the AACF should be constant for the straight-line motion of the pentosan flask-like colloidal motors, AACF = 1. As the motion behavior of the pentosan flask-like colloidal motors changes from ballistic motion to the enhanced Brownian motion,[41] the AACF decays exponentially in this stage. As shown in Fig. 2g, the AACF of the short-necked N100nm motors decays faster while the long-necked N600nm decays slower, indicating that the longer neck can decrease the rotation of pentosan flask-like colloidal motors during self-propelling motion. As schematically illustrated in Fig. 2h, the urease catalyzed reaction occurring inside the pentosan flask-like colloidal motors produces the gradient of the reactant (*i.e.* urea) and the products (*i.e.* CO_2 and NH_3) around the colloidal motor. Given that the pentosan flask-like colloidal motors move from the round bottom to the opening (Fig. 2a), the self-propelling force should be mainly ascribed to the urea concentration gradient, which is in agreement with the simulation of the urea concentration field around the pentosan flask-like colloidal motor (Fig. 2i) according to our previously reported method.[34] Briefly, the direction of the urea concentration gradient is from the opening to the round bottom, the self-propelled motion induced by the urease catalyzed reaction should be against the direction of the urea concentration gradient owing to the diffusiophoresis. Taken together, it can be found that, under the same reaction rate as shown in Fig. 1f, the increased neck length of the pentosan flask-like colloidal motors can reduce their rotation rate in the self-propelled motion and thus increase the directionality of the colloidal motors.

3.3. Contribution of translational and rotational motion

To better understand the underlying mechanism, we examined different dimensionless parameters similar to the Peclet (Pe) number, which can evaluate the relative importance between

the deterministic force like the self-propelling force and the stochastic force such as the Brownian force.[42] First, the translational motion resulting from the self-propelling force can be analysed as follows:

$$\mathrm{Pe}_{\mathrm{tran}} = \frac{a \times |v_{\mathrm{propel}}|}{D_0} \quad (3)$$

where $\mathrm{Pe}_{\mathrm{tran}}$ represents the Pe number that compares the ratio between the self-propelled motion and the translational Brownian motion, a is the characteristic length of the pentosan flask-like colloidal motors, $|v_{\mathrm{propel}}|$ is the modulus of the vector v_{propel} in different urea solutions, and D_0 is the translational diffusion coefficient of a passive pentosan flask-like colloidal particle in the solution with different urea concentrations, which is inversely proportional to the urea concentration shown in Fig. S2a (ESI†). As shown in Fig. 3a, the longer-necked pentosan flask-like colloidal motors have a larger value of $\mathrm{Pe}_{\mathrm{tran}}$ in the same urea solution, which corresponds to the larger self-propelling force translated from the chemical reaction. Meanwhile, the ratio between the translational and rotational motion, $\mathrm{Pe}_{\mathrm{tran-rot}}$, is described as follows:

$$\mathrm{Pe}_{\mathrm{tran\text{-}rot}} = \frac{|v_{\mathrm{propel}}|}{a \times D_{\mathrm{r}}} \quad (4)$$

where D_{r} is the rotational diffusion coefficient of the pentosan flask-like colloidal motors. According to eqn (4), in the 300 mM urea solution, the short-necked N100nm, the medium-necked N300nm and the long-necked N600nm motors have $\mathrm{Pe}_{\mathrm{tran\text{-}rot}}$ values of 38.36 ± 3.21, 46.52 ± 1.96 and 53.97 ± 1.75, respectively, indicating that the longer-necked pentosan flask-like colloidal motors have a larger value of $\mathrm{Pe}_{\mathrm{tran\text{-}rot}}$ (Fig. 3b). Therefore, the longer-necked pentosan flask-like colloidal motors can generate more translational force and thus the long-necked N600nm motors are able to move the straightest as shown in Fig. 2a. Furthermore, the relationship between the rotation of the pentosan flask-like colloidal motors and their neck lengths can be analyzed using the rotational friction coefficient ξ_{r},

$$\xi_{\mathrm{r}} = \frac{k_{\mathrm{B}}T}{D_{\mathrm{r}_0}} \quad (5)$$

where k_{B} is the Boltzmann constant, and T is the environmental temperature. D_{r_0} is the rotational diffusion coefficient caused by the Brownian motion of the pentosan flask-like colloidal particles, which is inversely proportional to the urea concentrations as shown in Fig. S2b (ESI†). Fig. 3c shows that the ξ_{r} values of short-necked N100nm, the medium-necked N300nm and the long-necked N600nm motors in the 300 mM urea solution are 2.37×10^{-21} Pa s m^3, 2.85×10^{-21} Pa s m^3 and 3.32×10^{-21} Pa s m^3, respectively. Obviously, the ξ_{r} value increases with the lengthening necks, which means the increased rotational drag of the longer-necked pentosan flask-like colloidal motors.

Finally, the energetic efficiency transferred from the chemical energy is an important parameter for evaluating the influence of the neck length.[43] The translational energetic efficiency η_{tran} can be characterized by the Stokes efficiency:[44]

$$\eta_{\mathrm{tran}} = \frac{\xi \langle v_{\mathrm{propel}} \rangle^2}{0.5 n_{\mathrm{NH_3}} \Delta_{\mathrm{r}}^{\theta} G} \quad (6)$$

where $n_{\mathrm{NH_3}}$ is the rate of NH_3 evolution each motor. $\Delta_{\mathrm{r}}^{\theta} G$ is the Gibbs free energy of the hydrolysis of urea into NH_3 and CO_2. ξ is the friction coefficient for the translational motion of the pentosan flask-like colloidal motors, which can be calculated from the Einstein–Smoluchowski equation:

$$\xi = \frac{k_{\mathrm{B}}T}{D_0} \quad (7)$$

The Stokes efficiency reveals how efficiently the pentosan flask-like colloidal motors can utilize the chemical free energy to drive the motors through the viscous medium. Fig. 3d shows that the η_{tran} values are proportional to the urea concentration, but the η_{tran} value of the short-necked N100nm motors is much smaller than that of the long-necked N600nm at the identical urea concentration. The finding reveals that the translational energetic efficiency η_{tran} increases with the lengthening neck; thus, the longer-necked pentosan flask-like colloidal motors can convert more energy into the translational motion and tend to move straighter.

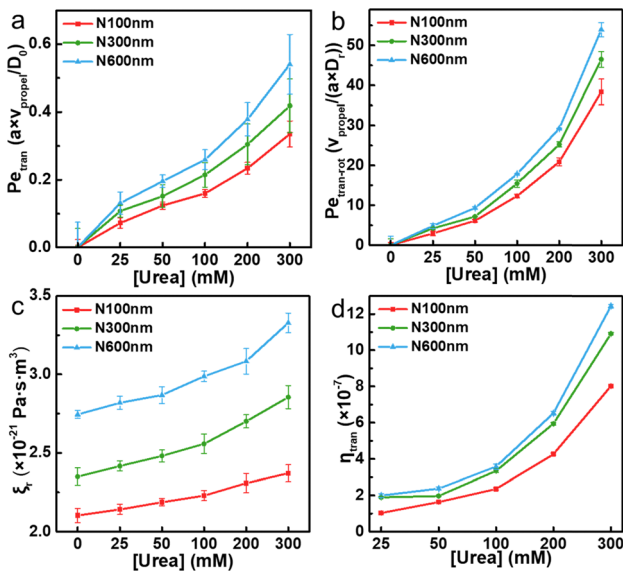

Fig. 3 The analysis of the ratio of the translation and rotation motion in the self-propelled motion of the pentosan flask-like colloidal motors. (a) The Pe number analysis for the translational motion. (b) The ratio of the translation and rotation in the self-propelled motion analyzed by the respective Pe number. (c) The rotational friction coefficient of the pentosan flask-like colloidal motors. (d) The energetic efficiency of the translational motion.

3.4. Mechanism and fluid flow field analysis

As mentioned above, the increasing self-propelled velocity is proportional to the neck length, which can be ascribed to the increased self-propelled component. To conduct theoretical analysis, we parameterize the geometry of the flask-like colloidal motors, as illustrated in Fig. 4a. The outer diameter of the round bottom and the opening are represented as $2R$ and d, respectively. The L represents the neck length. As shown above,

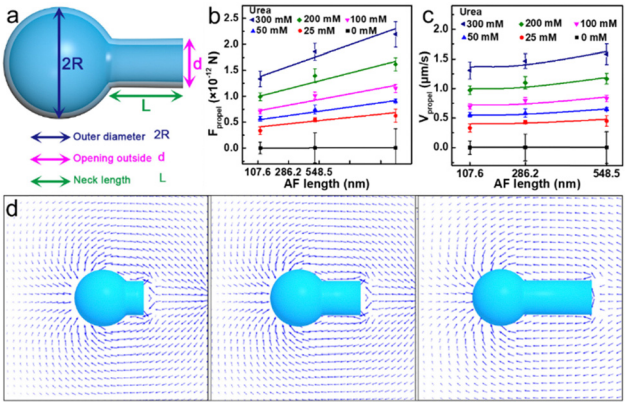

Fig. 4 The simulation of the self-propelled motion of the pentosan flask-like colloidal motors. (a) The scheme of the pentosan flask-like colloidal motors with corresponding parameters in the simulation. The self-propelled force (b) and the self-propelled velocity (c) with the fitting curves as a function of the neck length in different urea concentrations. (d) The fluid flow field around the pentosan flask-like colloidal motors.

R and d are both constant, which are 2.5×10^{-7} m and 2×10^{-7} m, respectively. The L is variable which varies from 1.076×10^{-7} m to 5.485×10^{-7} m. Furthermore, we assume that the tangential chemical gradient along the motor surface is constant, which is reasonable due to the small size of the motor. Thus, the self-propelled force is proportional to the effective surface area of the motor in the direction of its symmetric axis and can be roughly calculated as:

$$F_{\text{propel}} = \left(Ld + \frac{8}{3}R^2\right)\Delta \tag{10}$$

where Δ is a fitting parameter which represents the force per unit area. The term in the parentheses represents the force area. Through the data above, the calculated self-propelled force is proportional to the neck length as shown in Fig. 4b. By fitting the data in Fig. 4b through eqn (10), it can be found that the calculated F_{propel} is consistent with the experimental measurements, which can be deduced that the increase of F_{propel} is mainly contributed by the increase of the force area. Furthermore, the radius of the round bottom is almost twice than the opening, so the drag mainly arises from the round bottom; thus, it is similar for the pentosan flask-like colloidal motors with different neck lengths. Besides, under the condition with a low Reynold number, the inertia effect can be negligible; thus, the self-propelled force can be considered to be equal to the drag. Hence, the self-propelled velocity can be described by the following equation:

$$V_{\text{propel}} = \frac{\dfrac{F_{\text{propel}}}{L}}{3R + \dfrac{\ln\left(\dfrac{L}{d}\right) - 0.207 + \dfrac{0.98}{\dfrac{L}{d}} - \dfrac{0.133}{\left(\dfrac{L}{d}\right)^2}}} \tag{11}$$

where the denominator represents the friction coefficient.[45] By fitting the experimental self-propelled velocity as a function of the neck length according to eqn (11), it can be found that the calculated V_{propel} is consistent with the experimental data (Fig. 4c). Finally, through simulating the fluid flow field around the pentosan flask-like colloidal motors by using the fluent (Fig. 4d), it can be found that the amplitude of the flow around the neck is almost the same. However, there is more surface slip flow around the longer-necked pentosan flask-like colloidal motors, hence a larger self-propelled force, consistent with the above theoretical argument. Consequently, the larger self-propelled force and similar translational friction make the longer-necked pentosan flask-like colloidal motors move faster and straighter (larger rotational friction).

4. Conclusions

We have demonstrated that the self-propelled velocity of the pentosan flask-like colloidal motors is in proportion to the neck length while it is reversed for the randomly rotational speed which is due to the increased self-propelled force and rotational friction coefficient. The mechanism is that the increased trends of the self-propelled velocity with the longer neck length result from the increased self-propelled force and almost unchanged drag. With the lengthening of the neck, the force area increases; thus, the self-propelled force also shows an increasing trend. As the pentosan flask-like colloidal motors move from the bottom to the opening, the drag is proportional to the cross-sectional area perpendicular to the symmetric axis. The much larger area of the round bottom determines that the main drag consumption is concentrated here which results in the similar drag for the pentosan flask-like colloidal motors with different neck lengths. The increased self-propelled force and similar drag result in the increased self-propelled velocity and straighter motion. Meanwhile, the lengthening neck length enhances the rotational friction, which results in the decrease of rotational diffusion. These findings about the sub-micrometer-sized, streamlined, and urease-powered pentosan flask-like colloidal motors provide a proof-of-concept design for the colloidal motors to achieve the application of biomedicine and active drug delivery.

Author contributions

C. Zhou participated in experimental procedures. T. Y. Si and K. N. Zhu assisted with the data analysis. Y. J. Wu guided the research and wrote the manuscript. M. C. Yang performed the theoretical calculations. Q. He conceived the idea and guided the whole project. The manuscript was written through contributions of all authors.

Data availability

The data supporting this article are available within the article or its ESI.†

Conflicts of interest

There are no conflicts to declare.

Acknowledgements

This work was financially supported by the National Nature Science Foundation of China (22193033, 22172044, 12274448 and T2325027), the Key R&D Program of Heilongjiang Province, China (2022ZX02C23), and the start-up grant of Wenzhou Institute, University of Chinese Academy of Sciences (WIUCASQD2021044).

Notes and references

1 J. G. Mitchell, *Am. Nat.*, 2002, **160**, 727–740.
2 K. D. Young, *Microbiol. Mol. Biol. Rev.*, 2006, **70**, 660–703.
3 T. Kwon, N. Kumari, A. Kumar, J. Lim, C. Y. Son and I. S. Lee, *Angew. Chem., Int. Ed.*, 2021, **60**, 17579–17586.
4 S. Cao, H. Wu, I. A. B. Pijpers, J. Shao, L. K. E. A. Abdelmohsen, D. S. Williams and J. C. M. van Hest, *ACS Nano*, 2021, **15**, 18270–18278.
5 L. Wang, M. Marciello, M. Estévez-Gay, P. E. D. Soto Rodriguez, Y. Luengo Morato, J. Iglesias-Fernández, X. Huang, S. Osuna, M. Filice and S. Sánchez, *Angew. Chem., Int. Ed.*, 2020, **59**, 21080–21087.
6 D. Xu, J. Hu, X. Pan, S. Sánchez, X. Yan and X. Ma, *ACS Nano*, 2021, **15**, 11543–11554.
7 S. Kim, N. Kumari, J. Lim, S. Dubbu, A. Kumar and I. S. Lee, *Angew. Chem., Int. Ed.*, 2021, **60**, 16337–16342.
8 C. Hortelao Ana, C. Simó, M. Guix, S. Guallar-Garrido, E. Julián, D. Vilela, L. Rejc, P. Ramos-Cabrer, U. Cossío, V. Gómez-Vallejo, T. Patiño, J. Llop and S. Sánchez, *Sci. Robot.*, 2021, **6**, eabd2823.
9 M. Hansen-Bruhn, B. E.-F. de Ávila, M. Beltrán-Gastélum, J. Zhao, D. E. Ramírez-Herrera, P. Angsantikul, K. Vesterager Gothelf, L. Zhang and J. Wang, *Angew. Chem., Int. Ed.*, 2018, **57**, 2657–2661.
10 B. Esteban-Fernández de Ávila, D. E. Ramírez-Herrera, S. Campuzano, P. Angsantikul, L. Zhang and J. Wang, *ACS Nano*, 2017, **11**, 5367–5374.
11 J. Shao, S. Cao, D. S. Williams, L. K. E. A. Abdelmohsen and J. C. M. van Hest, *Angew. Chem., Int. Ed.*, 2020, **59**, 16918–16925.
12 V. M. Kadiri, C. Bussi, A. W. Holle, K. Son, H. Kwon, G. Schütz, M. G. Gutierrez and P. Fischer, *Adv. Mater.*, 2020, **32**, 2001114.
13 Z. Wang, D. Fu, D. Xie, S. Fu, J. Wu, S. Wang, F. Wang, Y. Ye, Y. Tu and F. Peng, *Adv. Funct. Mater.*, 2021, 2101648.
14 K. Khanvilkar, M. D. Donovan and D. R. Flanagan, *Adv. Drug Delivery Rev.*, 2001, **48**, 173–193.
15 C.-H. Heldin, K. Rubin, K. Pietras and A. Östman, *Nat. Rev. Cancer*, 2004, **4**, 806–813.
16 Y. Fu, F. Ye, X. Zhang, Y. He, X. Li, Y. Tang, J. Wang and D. Gao, *ACS Nano*, 2022, **16**, 18376–18389.
17 M. Wan, H. Chen, Q. Wang, Q. Niu, P. Xu, Y. Yu, T. Zhu, C. Mao and J. Shen, *Nat. Commun.*, 2019, **10**, 966.
18 A. Joseph, C. Contini, D. Cecchin, S. Nyberg, L. Ruiz-Perez, J. Gaitzsch, G. Fullstone, X. Tian, J. Azizi and J. Preston, *Sci. Adv.*, 2017, **3**, e1700362.
19 S. Tang, F. Zhang, H. Gong, F. Wei, J. Zhuang, E. Karshalev, B. Esteban-Fernández de Ávila, C. Huang, Z. Zhou, Z. Li, L. Yin, H. Dong, H. Fang Ronnie, X. Zhang, L. Zhang and J. Wang, *Sci. Robot.*, 2020, **5**, eaba6137.
20 J. Sun, M. Mathesh, W. Li and D. A. Wilson, *ACS Nano*, 2019, **13**, 10191–10200.
21 H. Choi, S. H. Cho and S. K. Hahn, *ACS Nano*, 2020, **14**, 6683–6692.
22 M. Wan, Z. Liu, T. Li, H. Chen, Q. Wang, T. Chen, Y. Tao and C. Mao, *Angew. Chem., Int. Ed.*, 2021, **60**, 16139–16148.
23 M. Wan, Q. Wang, R. Wang, R. Wu, T. Li, D. Fang, Y. Huang, Y. Yu, L. Fang, X. Wang, Y. Zhang, Z. Miao, B. Zhao, F. Wang, C. Mao, Q. Jiang, X. Xu and D. Shi, *Sci. Adv.*, 2020, **6**, eaaz9014.
24 J. Lin, C. Lian, L. Xu, Z. Li, Q. Guan, W. Wei, H. Dai and J. Guan, *Adv. Funct. Mater.*, 2024, 2417146.
25 Z. Yang, L. Wang, Z. Gao, X. Hao, M. Luo, Z. Yu and J. Guan, *ACS Nano*, 2023, **17**, 6023–6035.
26 X. Arqué, M. D. T. Torres, T. Patiño, A. Boaro, S. Sánchez and C. de la Fuente-Nunez, *ACS Nano*, 2022, **16**, 7547–7558.
27 C. Gao, Y. Wang, Z. Ye, Z. Lin, X. Ma and Q. He, *Adv. Mater.*, 2021, **33**, 2000512.
28 Z. Ye, Y. Wang, S. Liu, D. Xu, W. Wang and X. Ma, *J. Am. Chem. Soc.*, 2021, **143**, 15063–15072.
29 H. Chen, T. Shi, Y. Wang, Z. Liu, F. Liu, H. Zhang, X. Wang, Z. Miao, B. Liu, M. Wan, C. Mao and J. Wei, *J. Am. Chem. Soc.*, 2021, **143**, 12025–12037.
30 M. Liu, L. Chen, Z. Zhao, M. Liu, T. Zhao, Y. Ma, Q. Zhou, Y. S. Ibrahim, A. A. Elzatahry, X. Li and D. Zhao, *J. Am. Chem. Soc.*, 2022, **144**, 3892–3901.
31 C. Liu, J. Niu, T. Cui, J. Ren and X. Qu, *J. Am. Chem. Soc.*, 2022, **144**, 19611–19618.
32 F. Soto, E. Karshalev, F. Zhang, B. Esteban Fernandez de Avila, A. Nourhani and J. Wang, *Chem. Rev.*, 2021, **122**, 5365–5403.
33 J. Shao, S. Cao, H. Che, M. T. De Martino, H. Wu, L. K. E. A. Abdelmohsen and J. C. M. van Hest, *J. Am. Chem. Soc.*, 2022, **144**, 11246–11252.
34 C. Gao, C. Zhou, Z. Lin, M. Yang and Q. He, *ACS Nano*, 2019, **13**, 12758–12766.
35 C. Zhou, C. Gao, Y. Wu, T. Si, M. Yang and Q. He, *Angew. Chem., Int. Ed.*, 2022, **61**, e202116013.
36 C. Chen, H. Wang, C. Han, J. Deng, J. Wang, M. Li, M. Tang, H. Jin and Y. Wang, *J. Am. Chem. Soc.*, 2017, **139**, 2657–2663.
37 M. Tzaphlidou, J. A. Chapman and M. H. Al-Samman, *Micron*, 1982, **13**, 133–145.
38 X. Ma, A. Jannasch, U.-R. Albrecht, K. Hahn, A. Miguel-López, E. Schaffer and S. Sánchez, *Nano Lett.*, 2015, **15**, 7043–7050.
39 W. F. Paxton, K. C. Kistler, C. C. Olmeda, A. Sen, S. K. St. Angelo, Y. Cao, T. E. Mallouk, P. E. Lammert and V. H. Crespi, *J. Am. Chem. Soc.*, 2004, **126**, 13424–13431.
40 C. Krüger, G. Klös, C. Bahr and C. C. Maass, *Phys. Rev. Lett.*, 2016, **117**, 048003.
41 J. R. Howse, R. A. L. Jones, A. J. Ryan, T. Gough, R. Vafabakhsh and R. Golestanian, *Phys. Rev. Lett.*, 2007, **99**, 048102.
42 D. Schamel, A. G. Mark, J. G. Gibbs, C. Miksch, K. I. Morozov, A. M. Leshansky and P. Fischer, *ACS Nano*, 2014, **8**, 8794–8801.
43 N. Giuliani, L. Heltai and A. DeSimone, *Soft Rob.*, 2018, **5**, 410–424.
44 H. Wang and G. Oster, *Europhys. Lett.*, 2002, **57**, 134–140.
45 H. Löwen, *Phys. Rev. E: Stat. Phys., Plasmas, Fluids, Relat. Interdiscip. Top.*, 1994, **50**, 1232.

